

# Simultaneous measurement of nanoprobe indentation force and photoluminescence of InGaAs/GaAs quantum dots and its simulation

Yuan-Hua LIANG<sup>a</sup>, Yoshio ARAI<sup>a,\*</sup>, Kazunari OZASA<sup>b</sup>, Masane OHASHI<sup>a</sup>, Eiichiro TSUCHIDA<sup>a</sup>

<sup>a</sup>*Saitama University, 255 Shimo-Ohkubo, Sakura-ku, Saitama 338-0825, Japan*

<sup>b</sup>*The Institute of Physical and Chemical Research(RIKEN), 2-1 Hirosawa, Wako, Saitama 351-0198, Japan*

## ABSTRACT

Simultaneous measurement of the nanoprobe indentation force and the photoluminescence (PL) of In<sub>0.5</sub>Ga<sub>0.5</sub>As/GaAs quantum dots (QDs) is successfully achieved by introducing a specially designed loadcell into the nanoprobe indentation system. By using this improved system, the emission properties of self-assembled In<sub>0.5</sub>Ga<sub>0.5</sub>As/GaAs quantum dots (QDs) under nanoprobe indentation are investigated under low temperature and high vacuum conditions. Energy shifts as large as 90 meV induced by nanoprobe indentation are observed in the QDs. Further, the increase in the emission energy of the QDs varies from peak to peak under the same indentation force. In order to clarify this mechanism, simulations are carried out based on a three-dimensional finite element and six-band strain-dependent **k**·**p** Hamiltonian. The simulation results are in good agreement with the experimental ones. The results of the nanoprobe indentation experiments show that the change in the position of the QD relative to the nanoprobe results in a variation in its energy shift rate. This dependence of the energy shift rate of a QD on its position is also validated by repeated indentation with horizontal scan experiment.

\*Corresponding author: Yoshio ARAI, 255 Shimo-Ohkubo, Sakura-ku, Saitama 338-0825, Japan;

Tel: 048-858-3438; FAX: 048-856-2577; Email address: yarai@mech.saitama-u.ac.jp

*PACS:* 78.20.Hp; 78.66.Fd; 73.20.Dx; 78.55.-m

**Keywords:** Nanoprobe indentation; Quantum dots; Photoluminescence; Finite elements

## 1. INTRODUCTION

Self-assembled quantum dots (QDs), owing to their zero-dimensional confinements and consequently discrete energy spectra with  $\delta$ -like densities of states, have promising applications in electronic and optoelectronic devices [1, 2], such as semiconductor lasers [3-5], light emitting diodes [6, 7], single electron transistors [8, 9], and infrared detectors [10, 11]. One of the material pairs,  $\text{In}_x\text{Ga}_{1-x}\text{As}/\text{GaAs}$  QDs with various composition  $x$ , is an intense research topic since the  $\text{In}_x\text{Ga}_{1-x}\text{As}$  remains a direct-gap material over its entire composition range, suitable for laser diodes use based on double heterojunctions. By using  $\text{InGaAs}/\text{GaAs}$  QDs, Laser diodes with a lasing wavelength from 1100 nm to 1300 nm have been realized with particularly small threshold current densities and high temperature stability [12, 13].

In order to improve the performance of QD-based devices, it is important to control the discrete energy levels of QDs. The discrete energy levels of QDs can be tuned by external/internal strain; the shift in the emission wavelength produced by a strain-release capping layer has been reported for applications in telecommunication [14, 15], and the decrease in the splitting of fine structures by thermal annealing has been examined for potential implementation in quantum information systems [16]. A promising method for examining the effects of strain on the emission properties of QDs is to apply an external strain field by nanoprobe indentation. In recent experimental works, the application of nanoprobe indentation was found to produce large energy shifts in QDs [17-21]. Simulations suggested that these energy shifts were induced by the local strain field produced by nanoprobe indentation [19-21]. As compared with the strain-release capping layer and thermal annealing

techniques, the modulation of the discrete energy levels by nanoprobe indentation is more controllable and reproducible and can thus contribute significantly to the investigation and application of the optical and electronic properties of QDs [18, 19]. Unfortunately, in these works related to nanoprobe indentation [17-21], the quantitative understanding of the dependence of the energy level shifts of QDs on the external strain has been insufficient to realize the precise tuning of the energy levels of QDs. This is because the shapes of the tips of the probes were not fabricated precisely [17, 22, 23] or the three-dimensional shape/strain-field of the QDs was not reflected in two-dimensional analysis [19-21]. Additionally, the indentation force in these experiments was not measured directly, but estimated from the displacements of the nanoprobe and samples. A direct measurement of the indentation force with simultaneous observation of the discrete energy levels of the QDs is required for a high-accuracy strain/energy-level analysis, which can be used for strain design in device applications. For this purpose, a combined study of the precise fabrication of the apex of the nanoprobe, direct measurement of the indentation force, and quantitative analysis of the energy levels of QDs is essential.

In the present paper, we describe the simultaneous measurement of the indentation force and PL of  $\text{In}_{0.5}\text{Ga}_{0.5}\text{As}/\text{GaAs}$  QDs, together with experimental improvements on the precise fabrication of the nanoprobe. The simultaneous measurement of the indentation force and PL of QDs is achieved by introducing a sensitive loadcell into our previous nanoprobe indentation system [20, 21]. The nanoprobe is milled by FIB to obtain a flat apex aperture. Based on the quantitative relation between the nanoprobe indentation force and the discrete

energy levels of the QDs, which is determined experimentally, a theoretical analysis is performed based on a three-dimensional finite element calculation and six-band strain-dependent Hamiltonian. The distribution of biaxial strain under the central part of the nanoprobe and the contributions of the strain components to the energy shifts of the QDs are discussed from the analytical results.

## **2. EXPERIMENT**

The  $\text{In}_{0.5}\text{Ga}_{0.5}\text{As}$  QDs studied in the present work were prepared on GaAs(001) by chemical beam epitaxy [24, 25] and embedded in a 50 nm thick capping layer of GaAs. The configuration used for the nanoprobe PL measurement (Unisoku, USM-100R) was described previously, where a nanoprobe (Au-coated optical fiber) with a spherical apex rather than a flat apex was adopted [20, 21]. In the present experiment, however, the nanoprobe was milled by FIB to obtain a flat apex aperture with a radius of 425 nm (shown in the insert of Fig. 1). Then, the nanoprobe was installed to apply indentation force on the QD sample, and the PL of the sample was recorded through its aperture. A small cylindrical loadcell (aluminum alloy, Tokyo Sokki Kenkyujo) of the resistance-bridge type was specially designed for high sensitivity and for installation in the small sample holder of the nanoprobe PL system. With this loadcell below the QD sample, an indentation force as low as 200  $\mu\text{N}$  can be measured with good reproducibility. The experiments were carried out at a low temperature (10 K) and in an ultra-high vacuum ( $<1.4 \times 10^{-9}$  Pa).

After the abovementioned indentation experiments, the following unloading indentation experiments were performed in order to check for reversibility in our experiments. The

symmetry of the PL spectrum shifts of the QDs due to loading and unloading in our experiments indicated elastic deformation.

### 3. EXPERIMENTAL RESULTS

Fig. 1 shows the dependence of the indentation force on the nominal distance of the piezo-driven nanoprobe, as measured by the loadcell in a direction perpendicular to the sample surface. The nominal distance is estimated from the voltage applied to the probe-driving piezo-unit. The negative values of the nominal distance in Fig. 1 indicate the gap between the top surface of the QD sample and the flat apex of the nanoprobe, while positive values indicate the further downward displacement of the piezo-driven nanoprobe after the contact of the nanoprobe apex with the sample surface. The positive values comprise the deformation/displacement of the nanoprobe, the QD sample, and the loadcell. The zero point corresponds to the onset of the contact between the nanoprobe and the sample surface, determined by the emergence of the first sharp peak in the spectrum. From the linear fit in Fig. 1, we obtain the dependence of the PL spectrum shifts on the indentation force, as shown in Fig. 2(a). A vertical slice of this figure contains the PL spectrum for a given indentation force [18], and 58 spectra of this type comprise Fig. 2(a). The step-wise discontinuity in the diagram is a result of the enlargement of the indentation force axis, which is done to improve the visualization. The brightness in Fig. 2(a) corresponds to the PL peak intensity. The bright streaks show the shift of the emission energy of a single QD due to the nanoprobe indentation-induced strain. By tracing the typical bright streaks in Fig. 2(a), the shifts of the emission energy of the representative QDs are obtained as shown in Fig. 2(b). An energy shift

as large as 90 meV and its linear dependence on the indentation force are observed in Fig. 2(b). In order to present the difference in the shifts quantitatively, we define the shift rate of the emission energy as  $R_s = \frac{\Delta E}{\Delta F}$ , where  $\Delta E$  is the shift of the emission energy of the QD and  $\Delta F$  is the change of the indentation force. The value of  $R_s$  in Fig. 2(b) varies from 99 to 146 meV/mN.

The relatively large variation of  $R_s$  obtained can be clarified in a repeated indentation with the horizontal step-wise movement of the nanoprobe. In this repeated indentation experiment, the nanoprobe is gradually pressed downward onto the QD sample, and then lifted up and moved horizontally by 6.6 nm. This sequence is repeated eight times. The shifts of the emission energy of the QDs obtained in this experiment are shown in Fig. 3. Some of the bright streaks in Fig. 3 gradually change in shift rate according to the horizontal position of the nanoprobe. One streak of the emission energy, which is selected because of its strong dependence on the horizontal position of the nanoprobe, is traced by the dashed white lines in Fig. 3. As compared with this streak, the other bright streaks in Fig. 3 exhibit a weak dependence on the horizontal position of the nanoprobe. This difference in the dependence can be attributed to the variation in the local strain distribution, i.e., the relative position of the QDs and the nanoprobe, which will be discussed in Sec. 6.

#### **4. STRAIN ANALYSIS**

The strain field in and around the discussed QDs that is produced by the lattice mismatch and indentation force is analyzed by the finite element (FE) method. In the FE model, elastic anisotropy is adopted, and the material parameters of GaAs and  $\text{In}_{0.5}\text{Ga}_{0.5}\text{As}$  listed in Table 1

are used in the calculation [20, 26]. Here, we assume that the chemical composition of the QDs is uniform ( $\text{In}_{0.5}\text{Ga}_{0.5}\text{As}$ ) and the shape is pyramidal, with the (110) facets as a typical and ideal case, although the composition and shape of QDs depends on the growth conditions, including the growth temperature, growth rate, and capping process [27-30]. Some literatures also discussed the electronic structure consequences of nonuniformity of indium composition in self-assembled InGaAs/GaAs QDs through simulations [31-33]. The simulation work in Ref. 32 showed that the assumption of uniform indium distribution resulted in an approximate 1.4% overestimation of the ground state emission energy compared with the distribution-model for a truncated pyramidal  $\text{In}_{0.5}\text{Ga}_{0.5}\text{As}/\text{GaAs}$  QD, which indicated that the effect of In-distribution was adequately small compared with the ground-state emission energy discussed in this report. We also calculated the energy shift rates of QDs with a linear indium distribution of 74% at top and 44% at the base. The calculated energy shift rates along  $x$  axis were about 1 meV/mN smaller than those of the uniform In-distribution cases (shown in solid triangles in Fig.9). Therefore, we can reasonably neglect in our calculation the effects of nonuniform In-distribution by assuming the compositional uniformity for  $\text{In}_{0.5}\text{Ga}_{0.5}\text{As}$  QDs.

From microscopic observations [34], the base ( $2l$ ) and height ( $h$ ) of the pyramid-shaped QD are taken as 20 nm and 7 nm, respectively, as shown in Fig. 4. The thickness of the capping layer ( $t$ ) is 50 nm, and the diameter of the nanoprobe ( $2R$ ) is 850 nm. Due to the large size difference between the QD and the nanoprobe, the submodeling technique is used in the strain analysis. In the global indentation model, the QD sample is assumed to be



homogeneous GaAs since the size of the QD is considerably small when compared with the global model, whose dimensions are four times the radius of the nanoprobe ( $R$ ). Our calculations show that the dimensions of the global model are sufficiently large such that the influence of the surrounding traction-free boundary conditions in the indentation calculation can be neglected. A quarter of the nanoprobe indenter and the sample of GaAs are modeled based on the symmetry of the global model shown in Fig. 5(a). With respect to the coordinates shown in Fig. 4, the dimensions of the submodels used to simulate the QDs arraying along the  $x$  direction of the global model are 60 nm in the  $x$  direction, 30 nm in the  $y$  direction with respect to the symmetry plane  $x$ - $z$ , and 66 nm in the  $z$  direction, as shown in Fig. 5(b). Half of the QD is modeled in each submodel with respect to the symmetry plane  $x$ - $z$ , and its mesh is shown in the insert of Fig. 5(b). The size of the submodel is large enough to suppress the influences of the surrounding traction-free boundary conditions in the strain calculation, which are induced by lattice mismatch.

The indentation effects between the nanoprobe flat apex and top surface of the QD sample are calculated by using a small-sliding contact with no friction in the global model. Next, the results obtained using the global model are used to derive the surrounding displacement boundary conditions of the submodel. By using this submodeling technique, we obtain the indentation-induced strain field in and around the QD at any position along the  $x$  axis of the global model. The lattice-mismatched strain between the  $\text{In}_{0.5}\text{Ga}_{0.5}\text{As}$  QD and the GaAs matrix is calculated in the submodel according to Mura's theory on eigenstrain [35]. The lattice-mismatched QDs within the matrix can be assumed to be one type of inclusion for

a given eigenstrain, and the total strain  $e_{ij}$  is given by the sum of the eigenstrain  $\varepsilon_{ij}^*$  and the elastic strain  $\varepsilon_{ij}$ ,

$$e_{ij} = \varepsilon_{ij} + \varepsilon_{ij}^*, \quad (1)$$

where  $i$  and  $j$  take  $x$ ,  $y$ , or  $z$ . The eigenstrain due to the lattice mismatch,  $\varepsilon_{ij}^* = \varepsilon^* \delta_{ij}$ , can be calculated as

$$\varepsilon^* = \frac{a_{In_{0.5}Ga_{0.5}As} - a_{GaAs}}{a_{GaAs}} = 0.0358, \quad (2)$$

where  $\delta_{ij} = 1$  when  $i = j$  and  $\delta_{ij} = 0$  when  $i \neq j$ . In the FE calculation, the thermal expansion coefficients of the QD and the matrix are set as  $\varepsilon^*$  and 0, respectively, and the temperature of the submodel is raised by 1 K. Finally, the strain field in and around the QD, which is produced by the combination of the indentation force and lattice mismatch, is obtained by the summation of the indentation-induced strain and lattice-mismatch-induced strain.

The elastic strain components  $\varepsilon_{xx}$  and  $\varepsilon_{zz}$  in the QD sample due to the lattice mismatch and indentation force ( $F = 1.0$  mN) are shown in Fig. 6. In Fig. 6, the QD is located at  $x = 36$  nm, which is close to the center of the nanoprobe. In our calculation, the top surface of the sample is set at  $z = 0$  nm, as shown in Fig. 4; thus, the QD lies between  $z = 43$  and  $50$  nm (height 7 nm). In Fig. 6(a), a tensile strain is observed along the  $x$  direction ( $\varepsilon_{xx}$ ) in GaAs for  $z < 43$  nm or  $z > 50$  nm due to lattice mismatch. The compressive strain along the  $x$  direction in the QD is relaxed to approximately  $-0.029$  from the perfectly constrained mismatched strain of  $-0.0358$  because of the deformation of the GaAs matrix.

Compared with the influence exerted by indentation, the lattice mismatch has a predominant effect on the distribution of  $\varepsilon_{xx}$  in the QD. However, the influence of the indentation on  $\varepsilon_{zz}$  is comparable with the influence of the lattice mismatch, as shown in Fig. 6(b). Our calculation also suggests that the indentation force results in an approximate biaxial strain state under the center of the nanoprobe.

As in the general case for a biaxial strain state [36], the biaxial strain state can be divided into two parts, namely, the isotropic (hydrostatic) component  $\varepsilon_{hydro} = \varepsilon_{xx} + \varepsilon_{yy} + \varepsilon_{zz}$  and the average of the principal shear strain components in the  $x$ - $z$  and  $y$ - $z$  planes,  $\varepsilon_{shear} = \varepsilon_{zz} - \frac{1}{2}(\varepsilon_{xx} + \varepsilon_{yy})$ . The former only gives rise to a volume change without affecting the crystal symmetry; however, the latter usually decreases the symmetry of a strain-free crystal. In an indentation-induced compressive biaxial strain state, the hydrostatic component is primarily responsible for the upward shifting of the energy, especially in the conduction band. The average of the principal shear strain components, in the current ground state emission, produces a downward shift in the heavy-hole band and an upward shift in the light-hole band [18]. In addition, when the shear strain components exist in the coordinates of the crystal axes ( $\varepsilon_{ij} \neq 0, i \neq j$ ), they also contribute significantly to the shifting and splitting of the valence bands [37].

We examine the influence of the QD position on the strain field in and around the QD for  $x = 36$  nm (QD-A) and  $x = 414$  nm (QD-B). The former is almost under the center, while the latter is nearly below the edge of the nanoprobe. The components of the hydrostatic elastic strains ( $\varepsilon_{hydro}$ ) of QD-A and QD-B due to indentation are plotted in Fig. 7(a) and Fig. 7(b),

respectively. The hydrostatic strain under the center of the nanoprobe (QD-A in Fig. 7(a)) is almost homogeneous. On the contrary, the strain is distributed with a 20% change in magnitude when the QD is below the edge of the nanoprobe (QD-B in Fig. 7(b)). This is ascribed to the large gradient of the hydrostatic strain distribution below the edge of the contact area of the nanoprobe. The absolute value of the hydrostatic strain ( $\varepsilon_{hydro}$ ) in QD-A is larger than that in QD-B due to the strong constraint under the center of the contact area. Figs. 8(a) and 8(b) show the indentation-induced shear strain components ( $\varepsilon_{xz}$ ) of QD-A and QD-B, respectively. A large strain of 0.01 is obtained for  $\varepsilon_{xz}$  in QD-B; this value is close to zero in QD-A. As compared with  $\varepsilon_{hydro}$ ,  $\varepsilon_{xz}$  shows a considerable increase with a change in the position of the QD from the center to the edge of the nanoprobe. From the analysis, we also obtain the other strain components of QD-A and QD-B; however, their changes are not as large as those of the hydrostatic strain and shear strain of  $\varepsilon_{xz}$ .

The strain distribution obtained here suggests that the strain components of the QD are dependent on the relative position of the QD with respect to the nanoprobe. When the position of the QD shifts from the center to the edge of the nanoprobe, the compressive hydrostatic strain in the QD decreases by 0.005, while the shear strain of  $\varepsilon_{xz}$  increases by 0.01. This change in the strain field in and around the QD results in a change in the potential field in QD, as discussed in the following section.

## 5. ENERGY SHIFTS OF THE QDs

Based on the strain field obtained from the FE analysis, the strain-induced shifts of the discrete energy levels of the QD are calculated using the Pikus-Bir theory [38]. In this theory,

the elastic strain field is coupled to the quantum mechanical behavior of the charge carriers in semiconductors through the deformation potentials of the materials. For the valence band, the six-band strain-dependent Hamiltonian can be written as

$$H_{\varepsilon}^V = - \begin{bmatrix} P+Q & -S & R & 0 & \frac{\sqrt{1}}{2}S & -\sqrt{2}R \\ -S^* & P-Q & 0 & R & \sqrt{2}Q & -\frac{\sqrt{3}}{2}S \\ R^* & 0 & P-Q & S & -\frac{\sqrt{3}}{2}S^* & -\sqrt{2}Q \\ 0 & R^* & S^* & P+Q & \sqrt{2}R^* & \frac{\sqrt{1}}{2}S^* \\ \frac{\sqrt{1}}{2}S^* & \sqrt{2}Q & -\frac{\sqrt{3}}{2}S & \sqrt{2}R & P+\Delta_0 & 0 \\ -\sqrt{2}R^* & -\frac{\sqrt{3}}{2}S^* & -\sqrt{2}Q & \frac{\sqrt{1}}{2}S & 0 & P+\Delta_0 \end{bmatrix} \begin{matrix} \left| \frac{3}{2}, \frac{3}{2} \right\rangle \\ \left| \frac{3}{2}, \frac{1}{2} \right\rangle \\ \left| \frac{3}{2}, -\frac{1}{2} \right\rangle \\ \left| \frac{3}{2}, -\frac{3}{2} \right\rangle \\ \left| \frac{1}{2}, \frac{1}{2} \right\rangle \\ \left| \frac{1}{2}, -\frac{1}{2} \right\rangle \end{matrix}, \quad (3)$$

$$P = a_v (\varepsilon_{xx} + \varepsilon_{yy} + \varepsilon_{zz}), \quad Q = b \left[ \varepsilon_{zz} - \frac{1}{2} (\varepsilon_{xx} + \varepsilon_{yy}) \right],$$

$$R = \frac{\sqrt{3}}{2} b (\varepsilon_{xx} - \varepsilon_{yy}) - id \varepsilon_{xy}, \quad S = -d (\varepsilon_{xz} - i \varepsilon_{yz}),$$

where  $a_v$ ,  $b$ , and  $d$  are the hydrostatic and two shear deformation potentials, respectively;  $\Delta_0$  is the split-off energy gap [1, 39]. The elements indicated with an asterisk are the corresponding conjugate complexes. In principle, the Pikus-Bir strain Hamiltonian cannot be applied to non-uniformly distributed strain fields [40]. However, the strain distribution due to nanoprobe indentation discussed here is sufficiently small to support the applicability of the Pikus-Bir Hamiltonian. In  $\text{In}_{0.5}\text{Ga}_{0.5}\text{As}/\text{GaAs}$  QDs, the second conduction band has little effect on the first conduction band or valence band; therefore, the six-band, rather than the eight-band, strain-dependent Hamiltonian is adopted for simplicity. Thus, the shifts of the valence bands,  $\Delta E_v$ , are calculated as eigenvalues of  $H_{\varepsilon}^V$ :

$$\left| H_{\varepsilon}^V - \Delta E_v I \right| = 0, \quad (4)$$

where  $I$  is an identity matrix and  $| \cdot |$  denotes the determinant. For the conduction band of III-V semiconductors, the effect of a strain is to produce a hydrostatic energy shift

proportional to the fractional volume change, which is given by

$$\Delta E_c = a_c (\varepsilon_{xx} + \varepsilon_{yy} + \varepsilon_{zz}), \quad (5)$$

where  $a_c$  is the deformation potential of the conduction band [1].

In the present nanoprobe indentation experiments and simulations, the indentation-induced shifts of the emission energy exhibit values of up to 140 meV for a 1.0 mN indentation force. Since the size of the QD in the calculation is considerably smaller than the radius of the nanoprobe, the gradient of the indentation-induced strain field experienced by a single QD is considerably small (less than 20% in QD width). The GaAs surrounding the QD also exhibits a very similar energy shift behavior; consequently, the change in the confinement barrier is limited in our calculation. According to the results obtained by using the confinement energy with the approximation of a three-dimensional quantum box (not described in detail here), the indentation-induced energy shifts of the QDs are mainly determined by the indentation effects on the strain-induced potential change, and not by the strain-induced change in the confinement barrier (<2 meV). Thus, we can approximate the energy shifts of the QDs in these experiments as the difference between the shifts of the conduction band minimum (CBM) and the valence band maximum (VBM) of the QD, neglecting the quantum confinement effects. For the strain components at position  $(x, y, z)$ , the energy band gap shift is

$$\Delta E(x, y, z) = \Delta E_c(x, y, z) - \Delta E_v(x, y, z). \quad (6)$$

The energy band gap shift ( $\Delta E$ ) of a QD under indentation force ( $F$ ) is calculated based on the volume average assumption:

$$\Delta E = \frac{1}{V_0} \int_{V_0} \Delta E(x, y, z) dV, \quad (7)$$

where the volume integration is performed over the QD volume. This spatial averaging in our calculation is the same scheme adopted by Pryor et al [41], where they obtained reasonable results for the band-edge diagrams for strained III-V semiconductor quantum wells, wires and dots.

We now discuss the energy band gap shift rate ( $R_s$ ), defined in Sec. 2, on the basis of the simulation of the emission energy shift of the QDs at different positions relative to the nanoprobe. Fig. 9 shows the simulated dependence of the energy shift rates on the positions of the QDs along the  $x$  direction. The  $R_s$  of the QD increases slightly from the center to the edge, and reaches its maximum of 139 meV/mN around the edge of the contact area ( $\bar{r} \equiv x/R = 0.76$ ). It then decreases dramatically to 69 meV/mN at  $\bar{r} = 1.02$ , which is almost under the edge of the nanoprobe ( $\bar{r} = 1.0$ ). This variation of 69–139 meV/mN for the simulated rates agrees quantitatively with the variation observed in the experiments (typical bright streaks in Fig. 2(b)).

In Fig. 10, the shifts of the CBM and VBM of the QDs along the  $x$  axis are plotted. The strain induced by the lattice mismatch shifts the CBM and VBM upward by 281 meV and 56 meV, respectively, without any indentation. When the indentation-induced strain is superposed, the CBM for  $\bar{r} < 0.76$  shifts further upward by 101–106 meV, while the VBM for  $\bar{r} < 0.85$  shifts downward by 28–34 meV. In this superposition case, the CBM increases by only 5 meV when  $\bar{r}$  changes from 0 to 0.76, and it decreases rapidly by 47 meV for  $\bar{r}$

from 0.76 to 1.02. On the other hand, when  $\bar{r}$  changes from 0 to 0.85, the VBM decreases by 6 meV and reaches its minimum at  $\bar{r} = 0.85$  nm; it then increases rapidly by 25 meV for  $\bar{r}$  from 0.85 to 1.02. This indicates that the shift of the emission energy of the QD is reduced near the transitional area from the contact to the non-contact region, which agrees with the experimental observations for a small  $R_s$ , as shown in Fig. 2(b).

## 6. DISCUSSION

This section focuses on the analysis of the relation between the energy level shifts and indentation-induced strain states considering their position dependences. First, we consider the biaxial strain state, i.e.,  $\varepsilon_{xx} = \varepsilon_{yy} \neq \varepsilon_{zz}$  and  $\varepsilon_{xy} = \varepsilon_{yz} = \varepsilon_{zx} = 0$ , which is realized below the center of the nanoprobe. In this state, the nonzero elements in the six-band strain-dependent Hamiltonian are P and Q, as shown in Eq. (3); these relate to the hydrostatic strain and the average principal shear strain, respectively. From Eq. (3), the shifts of the valence bands are

$$\begin{cases} \Delta E_{hh} = -P - Q, \\ \Delta E_{lh} \approx -P + Q, \end{cases} \quad (8)$$

where  $\Delta E_{hh}$  and  $\Delta E_{lh}$  are the energy shifts of the heavy hole band and light hole band due to strain, respectively. In order to discuss the influence of the shear strain components of  $\varepsilon_{xz}$  on the shifting and splitting of the light hole and heavy hole bands, we should additionally consider a simple shear-strain state in which the only nonzero strain component is  $\varepsilon_{xz}$ . The substitution of this condition into Eq. (3) yields the dependence of the energy shift of the VBM ( $\Delta E_V$ ) on the shear strain components ( $\varepsilon_{xz}$ ):



$$\Delta E_V = \left[ -\frac{\Delta_0^3}{27} + \sqrt{\left(\frac{\Delta_0^3}{27}\right)^2 - \left(\frac{\Delta_0^2}{9} + (d\varepsilon_{xz})^2\right)^3} \right]^{\frac{1}{3}} + \left[ -\frac{\Delta_0^3}{27} - \sqrt{\left(\frac{\Delta_0^3}{27}\right)^2 - \left(\frac{\Delta_0^2}{9} + (d\varepsilon_{xz})^2\right)^3} \right]^{\frac{1}{3}} - \frac{\Delta_0}{3}. \quad (9)$$

Fig. 11 shows the changes in the volume-averaged  $-P$ ,  $-Q$  (Eq.(3)), and  $\Delta E_V$  (Eq. (9)) in the QD with its position from the center to the edge of the nanoprobe. The strain components adopted in Fig. 11 are from the FE analysis in Sec. 3. The dependence of  $-P$  and  $-Q$  on the QD position can be attributed to  $\varepsilon_{hydro}$  and  $\varepsilon_{shear}$  in the QD, respectively, as seen in Eq. (3). The dependence of  $\Delta E_V$  in Fig. 11 can be related directly to  $\varepsilon_{xz}$ , as indicated in Eq. (9). In Fig. 11, the values of  $-P$  and  $\Delta E_V$  are almost independent of the QD position when  $\bar{r} < 0.76$ . When  $\bar{r}$  changes from 0.76 to 1.02, the value of  $-P$  increases from  $-16$  meV to  $-9$  meV, and  $\Delta E_V$  increases from 1 meV to 43 meV. On the other hand, the value of  $-Q$  decreases slowly when  $\bar{r}$  changes from 0 to 0.93 (down to its minimum value of  $-28$  meV at  $\bar{r} = 0.93$ ), and then increases rapidly to  $-11$  meV when  $\bar{r}$  changes from 0.93 to 1.02.

The dependence of  $-P$ ,  $-Q$ , and  $\Delta E_V$  in Fig. 11 corresponds to the strain distribution shown in Fig. 7 and Fig. 8. In both the QDs, the sign of the indentation-induced  $\varepsilon_{hydro}$  is negative below the center (Fig. 7(a)) and edge of the nanoprobe (Fig. 7(b)). Due to the different constraint condition of the compressive region, the absolute value of  $\varepsilon_{hydro}$  of the QD when it is close to the center is larger by 0.004~0.005 than when it is near the edge. Consequently, the upward shift of the CBM of the QD when it is close to the center is 25~30 meV larger than when it is near the edge (Eq. (5) and Fig. 10). The difference in  $\varepsilon_{hydro}$  also causes a similar behavior of the VBM: the downward shift of the VBM of the QD when it is

close to the center is 4~5 meV larger than when it is near the edge (Eq. (8)). Since the absolute value of the deformation potential of  $a_v$  is considerably smaller than that of  $a_c$ , the downward shift of the VBM caused by  $\varepsilon_{hydro}$  is only 15% of the upward shift of the CBM. As shown in Fig. 8, the shear strain component  $\varepsilon_{xz}$  increases from approximately zero to 0.01 when the position of the QD shifts from the center to the edge of the nanoprobe, which results in a 38 meV upward shift of the VBM according to Eq. (9). This increase in  $\varepsilon_{xz}$  causes a larger upward shift of the VBM of the QD when it is near the edge than when it is close to the center of the nanoprobe ( $\Delta E_v$  in Fig. 11); this causes a reduction in the emission energy of the QD when it is at the edge.

The shifts of the CBM and VBM due to indentation are summarized in Fig. 12, with the normalization of the energy shifts by  $\overline{\Delta E}_0 \equiv (a_c + a_v) \frac{F}{\pi R^2 E_{eff}}$ , where  $a_c$  and  $a_v$  are the deformation potentials of the  $\text{In}_{0.5}\text{Ga}_{0.5}\text{As}$  QD;  $F$ , the indentation force;  $R$ , the radius of the indenter; and  $E_{eff}$ , the equivalent Young's modulus of  $\text{In}_{0.5}\text{Ga}_{0.5}\text{As}$ . From the above discussion and the dependences shown in Fig. 12, we can deduce the following relationship between the indentation-induced strain state and the energy shifts of the CBM and VBM of the QD.

(a) The compressive hydrostatic strain is weakly dependent on the QD position when  $\bar{r} < 0.76$ , while the absolute value of the hydrostatic strain decreases significantly because of the loss of constraint in the surrounding material for  $\bar{r}$  from 0.76 to 1.02. This decrease reduces the upward shift of the CBM with the deformation potential of  $a_c$ . Similarly, it reduces the downward-shift of the VBM with the deformation potential of  $a_v$ .

(b) The shear strain component of  $\varepsilon_{xz}$  also has a weak dependence on the QD position when  $\bar{r} < 0.76$ . It increases by 0.01 when  $\bar{r}$  changes from 0.76 to 1.02 due to the evolution of shear strain around the edge of the nanoprobe. This increase results in a large upward shift of the VBM, which significantly narrows the band gap of the QD and consequently decreases the shift rate of the energy band gap,  $R_s$ .

(c) The principal shear strain causes a gradual downward shift of the VBM by 12 meV when  $\bar{r}$  ranges from 0 to 0.93, and an upward shift by 17 meV when  $\bar{r}$  ranges from 0.93 to 1.02. Due to the combined effect of the shifts of the VBM and CBM, the maximum energy shift rates are observed at  $\bar{r} = 0.76$ , instead of at the center of the nanoprobe. In addition, the upward shift of the VBM for  $\bar{r}$  from 0.93 to 1.02 due to the principal shear strain contributes partly to the decrease in the energy shift rates of the QD near the edge of the nanoprobe.

## 7. CONCLUSION

In this work, the simultaneous measurement of the nanoprobe indentation force and the photoluminescence of QDs was successfully achieved in nanoprobe indentation experiments; the results yielded information essential for the precise description of the effects of external strain on the energy levels of QDs. Based on the precisely determined indentation force, quantitative agreements were obtained between the simulations and the experiments for the energy shifts of QDs that were produced using a nanoprobe. The shifts of the emission energy of QDs under the center of the nanoprobe ( $\bar{r} < 0.76$ ) were attributed mainly to the increase in the CBM (78%) rather than the decrease in the VBM (22%). Under the edge of the

nanoprobe-indentured area, the decrease in the VBM was reduced to almost zero, but the increase in the CBM still remained at over 50% of that at the center. These results revealed that the increase in the strain component  $\varepsilon_{xz}$  at the edge of the nanoprobe is responsible for the upward shift of the VBM, while the loss of constraint at the edge results in a reduction in the upward shift of the CBM. Simultaneous measurements of the nanoprobe indentation force and the PL of QDs enables us to modulate the discrete energy levels of the QDs precisely and reproducibly. It provides a promising method of studying the emission properties of QDs due to strain and to realize the strain-based modulation of the energy levels in QDs in various applications.

Acknowledgements: This research was partially supported by the Ministry of Education, Science, Sports and Culture of Japanese Government, Grant-in-Aid for Scientific Research (C), 16560060, 2004 – 2005. One of the authors (Y. H. Liang) gratefully acknowledges the scholarship from the Ministry of Education, Science, Sports and Culture of Japanese Government during the research.

## REFERENCES

- [1] D. Bimberg, M. Grundmann, N. N. Ledentsov, Quantum Dot Heterostructures. Wiley, London, 1998.
- [2] T. J. Bukowski, J. H. Simmons, 2002. Critical Reviews in Solid State and Materials Sciences 27 (2002) 119.
- [3] D. L. Huffaker, G. Park, Z. Zou, O. B. Shchekin, and D. G. Deppe, Appl. Phys. Lett. 73 (1998) 2564.
- [4] G. T. Liu, A. Stintz, H. Li, T. C. Newell, A. L. Gray, P. M. Varangis, K. J. Malloy, and L. F. Lester, IEEE J. Quantum Electron. 36 (2000) 1272.
- [5] A. Wilk, A.R. Kovsh, S.S. Mikhlin, C. Chaix, I.I. Novikov, M.V. Maximov, Yu.M. Shernyakov, V.M. Ustinov and N.N. Ledentsov, 2005, J. Cryst. Growth 278 (2005) 335.
- [6] A. Krier, X. L. Huang, Physica E 15 (2002) 159.
- [7] L. -W. Ji, Y. K. Su, S. J. Chang, C. S. Chang, L. W. Wu, W. C. Lai, X. L. Du and H. Chen, J. of Crystal Growth 263 (2004) 114.
- [8] B. H. Choi, S. H. Son, K. H. Cho, S. W. Hwang, D. Ahn, D. H. Kim, J. D. Lee and B. G. Park, Microelectronic Engineering 63 (2002) 129.
- [9] K. D. Osborn, Mark W. Keller and R. P. Mirin, Physica E 21 (2004) 501.
- [10] J. Stangl, V. Holy, G. Bauer, Rev. Mod. Phys. 76 (2004) 725.
- [11] S.H. Hwang, J.C. Shin, J.D. Song, W.J. Choi, J.I. Lee, H. Han and S.-W. Lee, Microelectronic Engineering 78-79 (2005) 229.
- [12] M. Grundmann, Physica E. 5 (2000) 167.
- [13] M. Grundmann, F. Heinrichsdorff, N. N. Ledentsov, C. Ribbat, D. Bimberg, A. E. Zhukov, A. R. Kovsh, M. V. Maximov, Y. M. Shernyakov, D. A. Lifshits, V. M. Ustinov and Z. I. Alferov, Jpn. J. Appl. Phys. 39 (2000) 2341.
- [14] J. X. Chen, A. Markus, A. Fiore, U. Oesterle, R. P. Stanley, J. F. Carlin, R. Houdre, M. Ilegems, L. Lazzarini, L. Nasi, M. T. Todaro, E. Piscopiello, R. Cingolani, M. Catalano, J. Katecki and J. Ratajczak, J. Appl. Phys. 91 (2002) 6710.
- [15] F. Guffarth, R. Heitz, A. Schliwa, O. Stier, N. N. Ledentsov, A. R. Kovsh, V. M. Ustinov, and D. Bimberg, Phys. Rev. B 64 (2001) 085305.
- [16] A. I. Tartakovskii, M. N. Makhonin, I. R. Sellers, J. Cahill, A. D. Andreev, D. M. Whittaker, J-P. R. Wells, A. M. Fox, D. J. Mowbray, M. S. Skolnick, K. M. Groom, M. J. Steer, H. Y. Liu, and M. Hopkinson, Phys. Rev. B 70 (2004) 193303.
- [17] H. D. Robinson, M. G. Muller, B. B. Goldberg, Appl. Phys. Lett. 72 (1998) 2081.
- [18] A. Chavez-Pirson, J. Temmyo, H. Ando, Physica E 7 (2000) 367.
- [19] A. M. Mintairov, K. Sun, J. L. Merz, C. Li, A. S. Vlasov, D. A. Vinokurov, O. V. Kovalenkov, V. Tokranov, S. Oktyabrsky, Phys. Rev. B 69 (2004) 155306.
- [20] K. Ozasa, Y. Aoyagi, A. Yamane, Y. Arai, Appl. Phys. Lett. 83 (2003) 2247.
- [21] K. Ozasa, Y. Aoyagi, M. Hara, M. Maeda, A. Yamane, Y. Arai, Physica E 21 (2004) 265.
- [22] H. T. Johnson, R. Bose, B. B. Goldberg, H. D. Robinson, Int. J. Multiscale Computational Engineering. 1 (2003) 33.

- [23] H. T. Johnson, R. Bose, *J. Mech. Phys. Sol.* 51 (2003) 2085.
- [24] K. Ozasa, Y. Aoyagi, Y. J. Park, L. Samuelson, *Appl. Phys. Lett.* 71 (1997) 797.
- [25] K. Ozasa, Y. Aoyagi, *J. Cryst. Growth* 188 (1998) 370.
- [26] S. Adachi, *J. Appl. Phys.* 53 (1982) 8775.
- [27] D. M. Bruls, J. W. A. M. Vugs, P. M. Koenraad, H. W. M. Salemink, J. H. Wolter, M. Hopkinson, M. S. Skolnick, F. Long, S. P. A. Gill, *Appl. Phys. Lett.* 81 (2002) 1708.
- [28] C.H. Hsu, H.Y. Lee, Y.W. Hsieh, Y.P. Stetsko, M.T. Tang, K.S. Liang, N.T. Yeh, J.I. Chyi, D.Y. Noh, *Physica B* 336 (2003) 98.
- [29] A. Lemaître, G. Patriarche, F. Glas, *Appl. Phys. Lett.* 85 (2004) 3717.
- [30] V. G. Dubrovskii, G. E. Cirlin, Yu. G. Musikhin, Yu. B. Samsonenko, A. A. Tonkikh, N. K. Polyakov, V. A. Egorov, A. F. Tsatsul'nikov, N. A. Krizhanovskaya, V. M. Ustinov and P. Werner, *J. Cryst. Growth* 267 (2004) 47.
- [31] A. J. Williamson, L. W. Wang and A. Zunger, *Phys. Rev. B* 62 (2000) 13963.
- [32] J. Shumway, A. J. Williamson, A. Zunger, A. Passaseo, M. DeGiorgi, R. Cingolani, M. Catalano and P. Crozier, *Phys. Rev. B* 64 (2001) 125302.
- [33] G. Bester and A. Zunger, *Phys. Rev. B* 68 (2003) 073309.
- [34] K. Ozasa, Y. Aoyagi, M. Iwaki, H. Kurata, *J. Appl. Phys.* 94 (2003) 313.
- [35] T. Mura, *Micromechanics of defects in solids*, Second revised version, Martinus Nijhoff Publishers, Boston, 1987.
- [36] J. Singh, *Strain-induced bandstructure modifications in semiconductor heterostructures- Consequences for optical properties and optoelectronic Devices. Handbook on Semiconductors (2)*, edited by M. Balkanski, North-Holland, 1994.
- [37] F. H. Pollak, M. Cardona, *Phys. Rev.* 172 (1968) 816.
- [38] G. L. Bir, G. E. Pikus, *Symmetry and Strain-Induced Effects in Semiconductors*. Wiley, New York, 1974.
- [39] J. Singh, *Physics of semiconductors and their Heterostructures*, McGraw-Hill, Inc. New York, 1993.
- [40] T. Suzuki, *Phys. Rev. B*, 64 (2000) 233310.
- [41] C. E. Pryor and M.-E. Pistol, *Phys. Rev. B* 72, (2005) 205311.

## Figure captions

- Fig.1** Dependence of indentation force on z step of the piezo-driven nanoprobe in nanoprobe indentation experiment. The milled flat apex of nanoprobe is shown in the insert.
- Fig.2** Dependence of energy band gap shifts of QDs on indentation force. (a) Indentation force dependence of nanoprobe PL spectrum. The brightness in the figure shows the intensity of peak. (b) Traces of some emission lines in (a). Values are the energy shift rates of each peak.
- Fig.3** Shifts of emission energy from QDs in the experiment of repeated indentation with horizontal step-wise movement of nanoprobe. The dashed white lines in the figure are corresponding to the shift of emission energy of one QD at different position relative to the nanoprobe.
- Fig. 4** Illustration of the simulation model in the nanoprobe indentation (not to scale)
- Fig. 5** Illustration of the FE mesh used in 3D contact simulation. (a)The mesh of the global model, (b) the mesh of submodel along x axis, half of the QD is modeled due to the symmetry. This model was also used for lattice mismatched strain calculation.
- Fig. 6** Distribution of elastic strain in and around QD due to lattice mismatch and indentation. (a) Distribution of  $\varepsilon_{xx}$  through the centre of the QD, which is along A-A in Fig.(4). (b) Distribution of  $\varepsilon_{zz}$  through the centre of the QD, which is along A-A in Fig.(4).
- Fig. 7** Distribution of elastic hydrostatic strain in and around QD due to 1.0 mN indentation force with 425 nm radius indenter. (a) QD at x=36 nm, (b) QD at x=414 nm.
- Fig. 8** Distribution of  $\varepsilon_{xz}$  in and around QD due to 1.0 mN indentation force with 425 nm radius indenter. (a) QD at x=36 nm, (b) QD at x=414 nm.
- Fig. 9** Dependence of the energy shift rates on the position of the QD along x direction.
- Fig. 10** Dependence of energy shift of conduction band minimum (CBM) and valence band maximum (VBM) on the position of the QD along x axis.
- Fig. 11** Dependence of -P, -Q and  $\Delta E_v$  on the position of the QD due to 1.0 mN indentation force.
- Fig. 12** Dependence of shifts of the CBM and the VBM on the position of the QD, the shifts are the difference of lattice mismatch case and superposition of indentation force with lattice mismatch case.

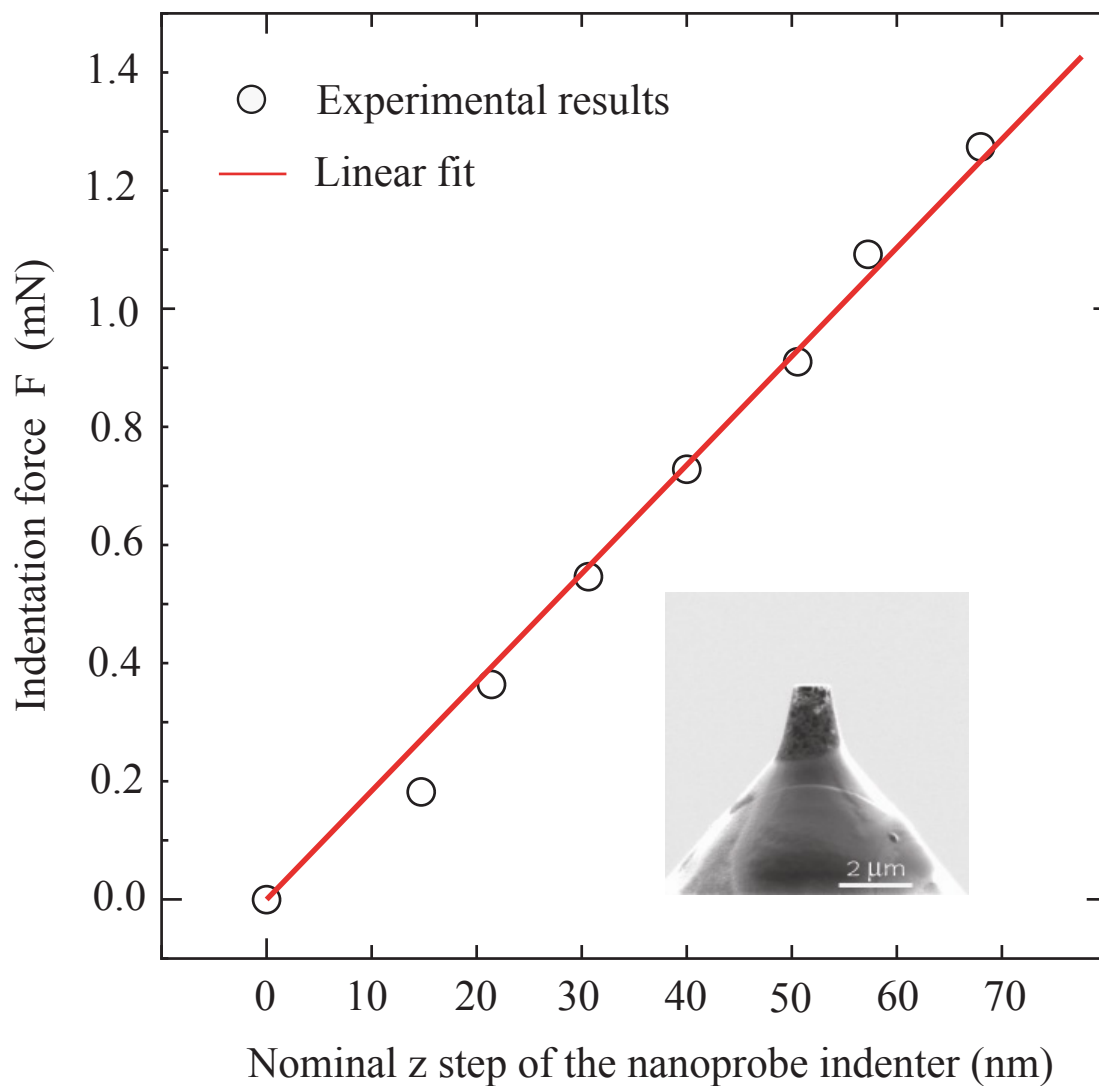
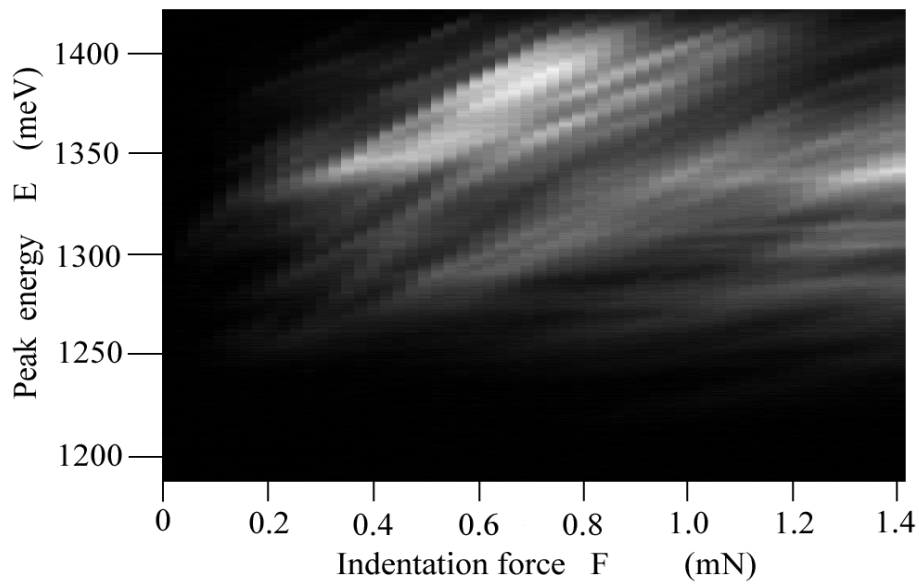
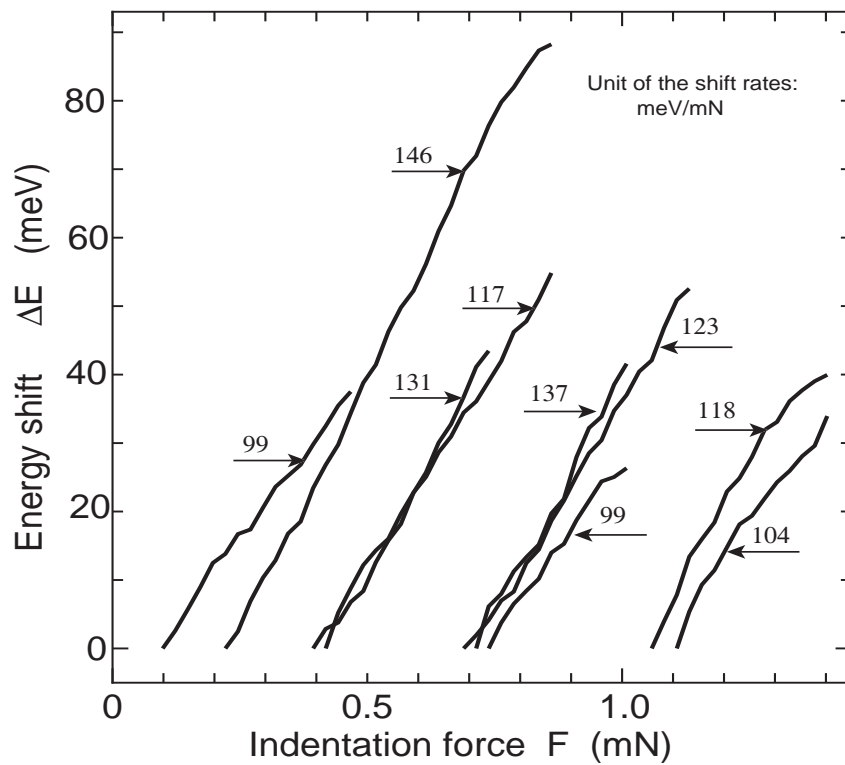


**Fig.1 Dependence of indentation force on z step of the piezo-driven nanoprobe in nanoprobe indentation experiment. The milled flat apex of nanoprobe is shown in the insert.**





(a)



(b)

**Fig.2 Dependence of energy band gap shifts of QDs on indentation force. (a) Indentation force dependence of nanoprobe PL spectrum. The brightness in the figure shows the intensity of peak. (b) Traces of some emission lines in (a). Values are the energy shift rates of each peak.**

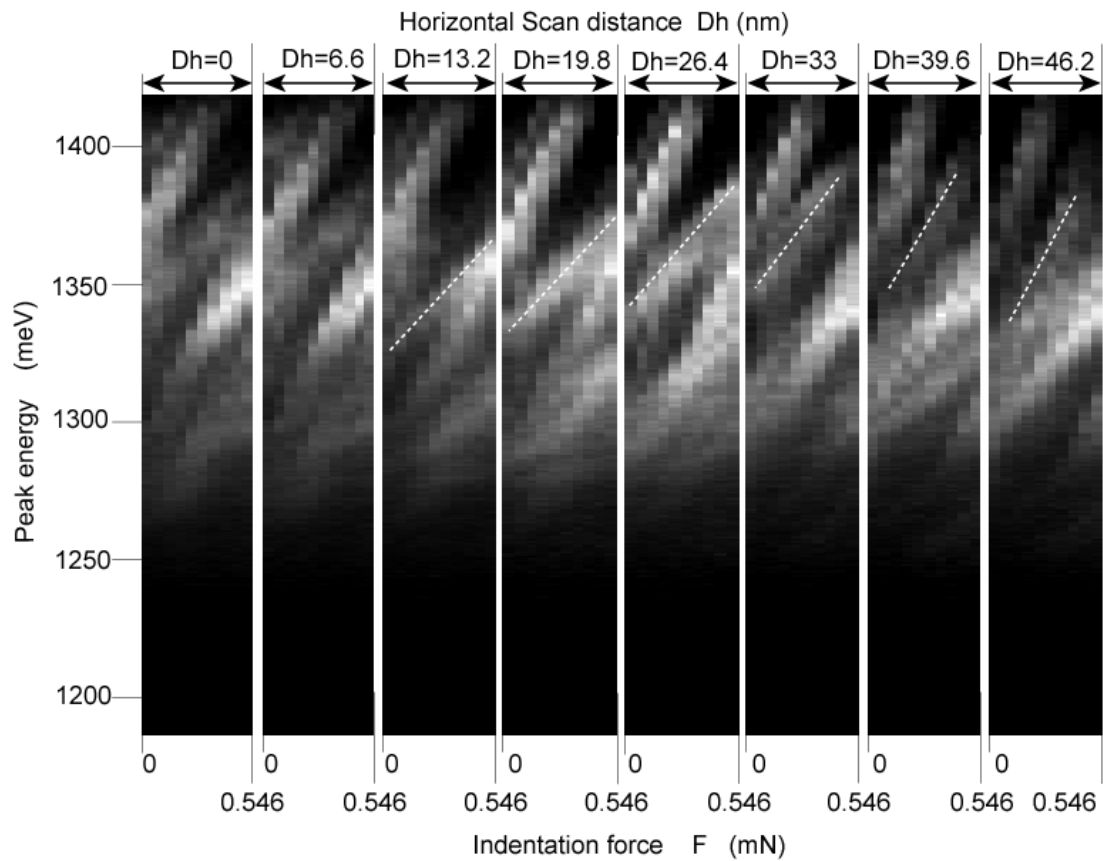


**Fig.3 Shifts of emission energy from QDs in the experiment of repeated indentation with horizontal step-wise movement of nanoprobe. The dashed white lines in the figure are corresponding to the shift of emission energy of one QD at different position relative to the nanoprobe.**

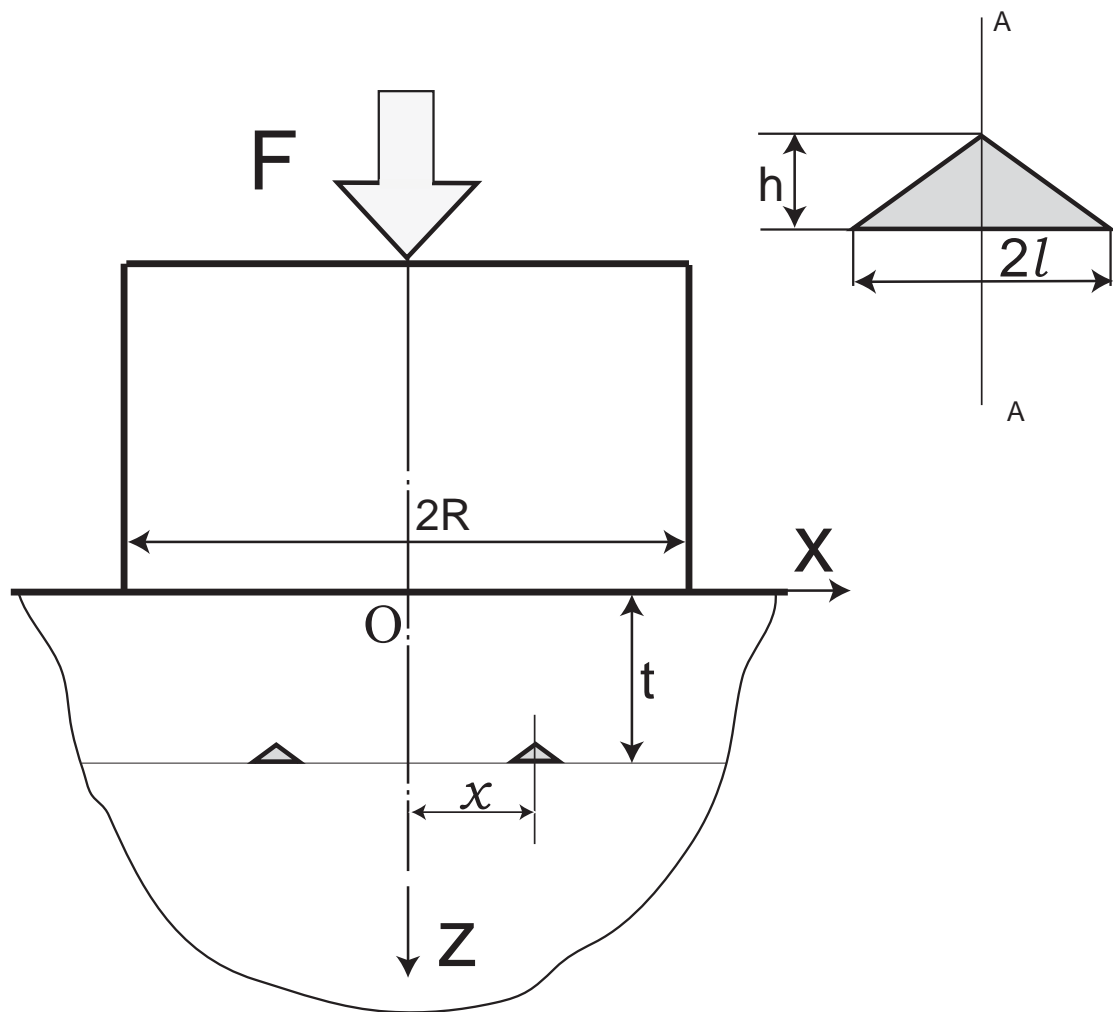
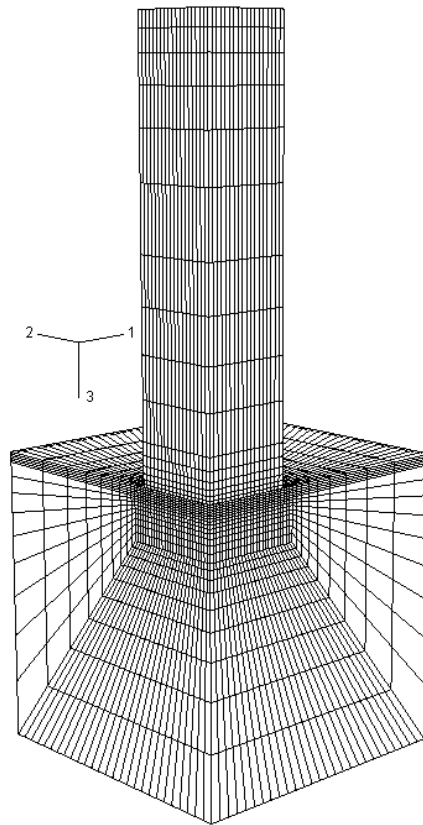
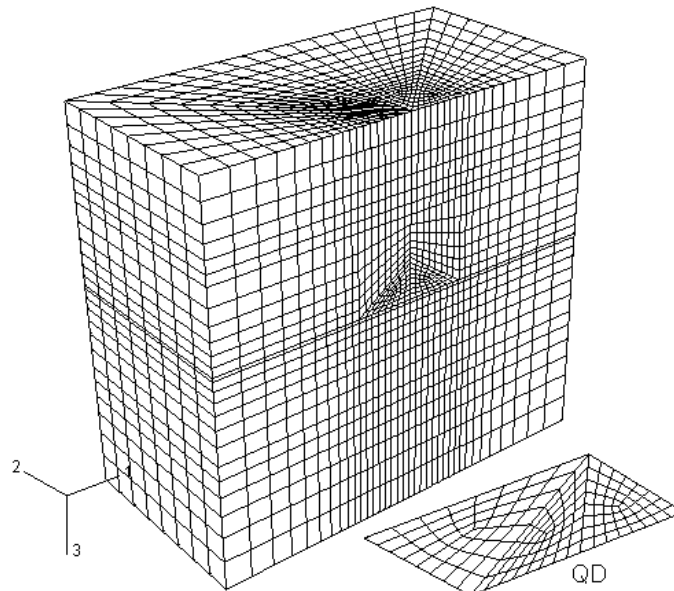


**Fig. 4 Illustration of the simulation model in the nanoprobe indentation (not to scale)**

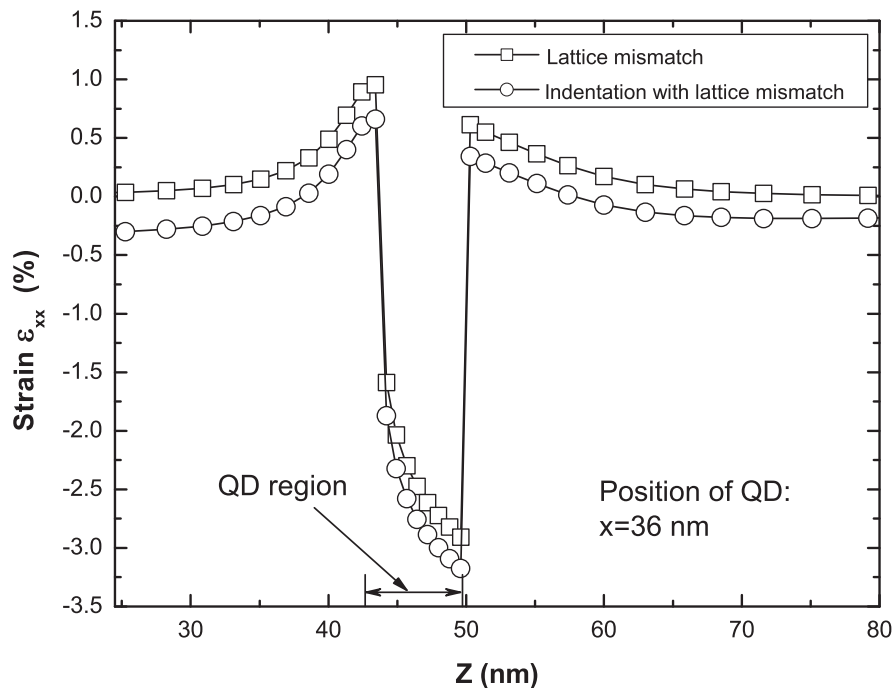


(a)

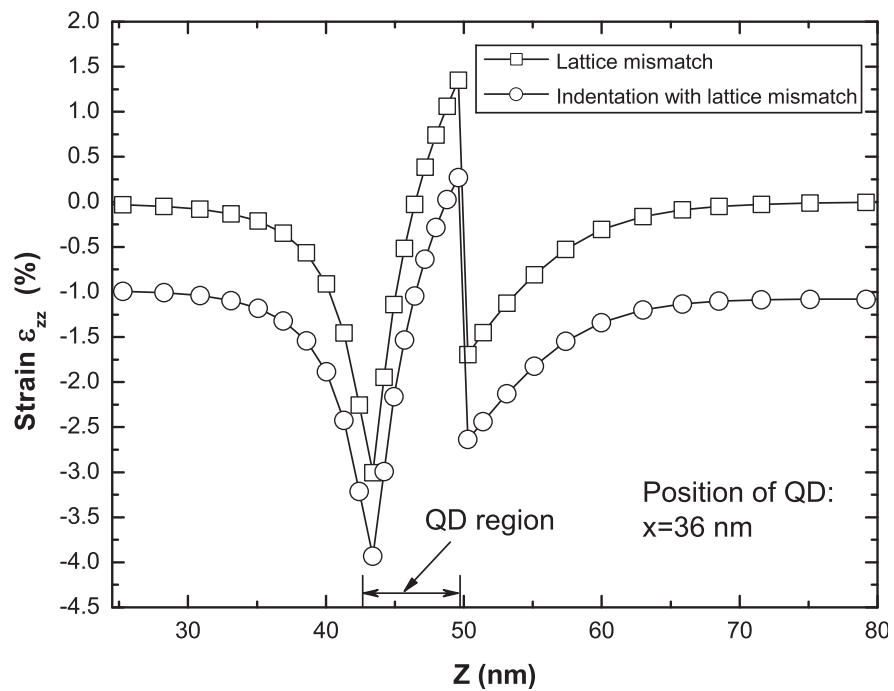


(b)

**Fig. 5 Illustration of the FE mesh used in 3D contact simulation. (a)The mesh of the global model, (b) the mesh of submodel along x axis, half of the QD is modeled due to the symmetry. This model was also used for lattice mismatched strain calculation.**

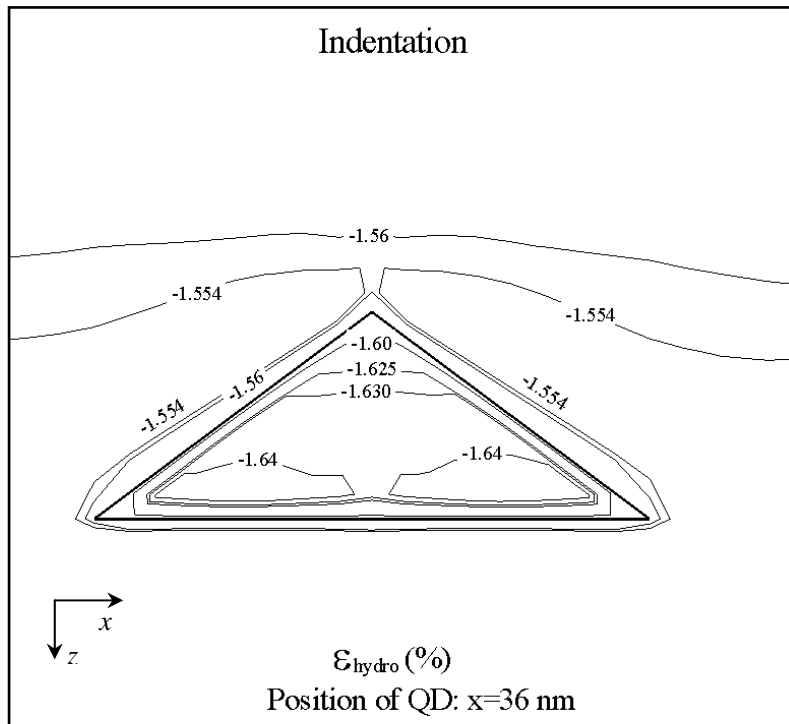


(a)

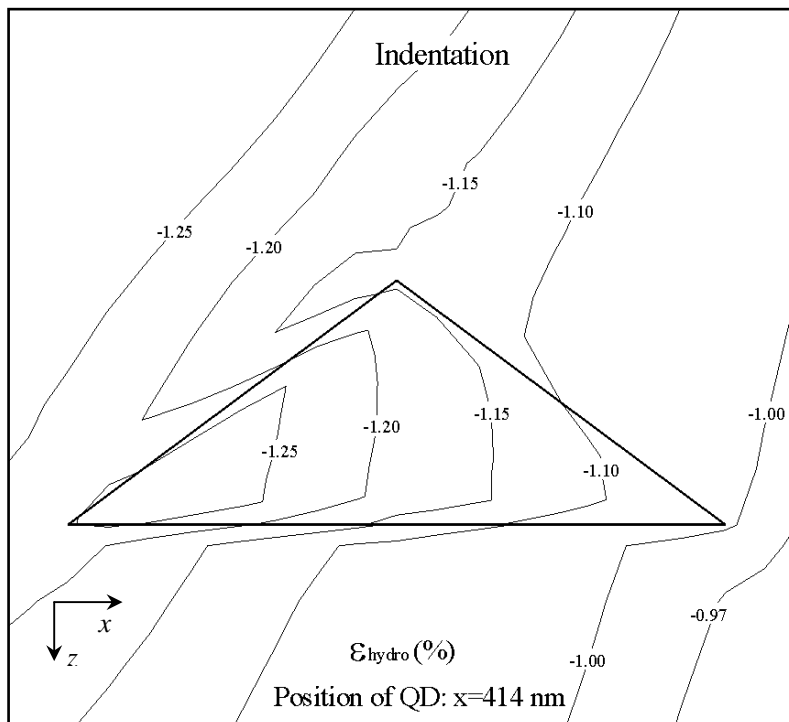


(b)

**Fig. 6 Distribution of elastic strain in and around QD due to lattice mismatch and indentation. (a) Distribution of  $\epsilon_{xx}$  through the centre of the QD, which is along A-A in Fig.(4). (b) Distribution of  $\epsilon_{zz}$  through the centre of the QD, which is along A-A in Fig.(4).**

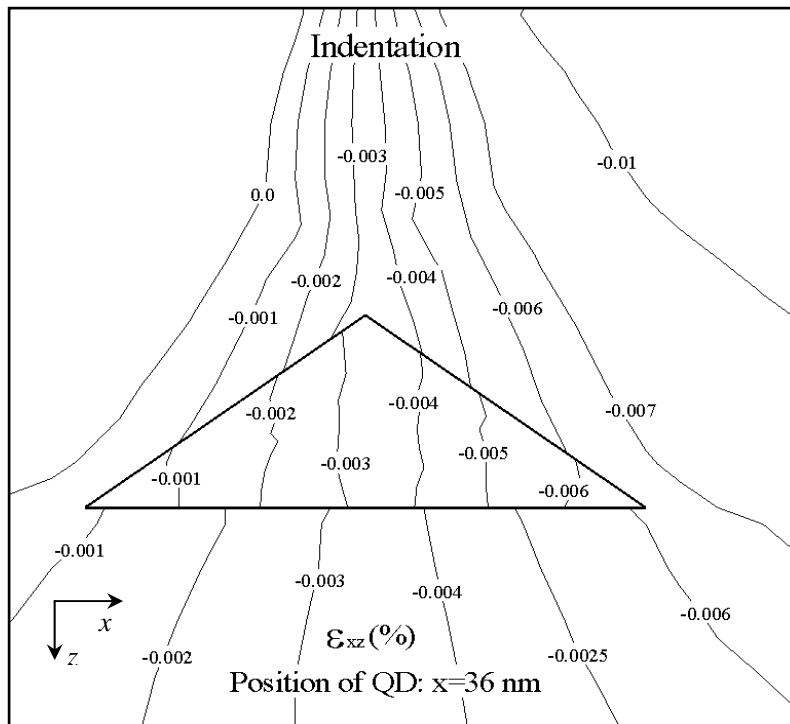


(a)

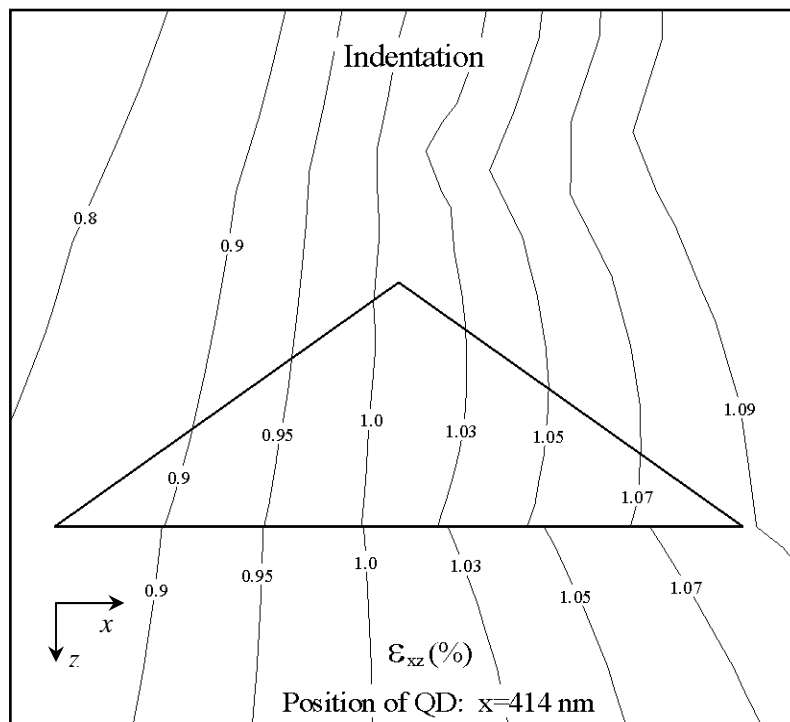


(b)

**Fig. 7** Distribution of elastic hydrostatic strain in and around QD due to 1.0 mN indentation force with 425 nm radius indenter. (a) QD at  $x=36 \text{ nm}$ , (b) QD at  $x=414 \text{ nm}$ .



(a)



(b)

**Fig. 8 Distribution of  $\epsilon_{xz}$  in and around QD due to 1.0 mN indentation force with 425 nm radius indenter. (a) QD at  $x=36$  nm, (b) QD at  $x=414$  nm.**

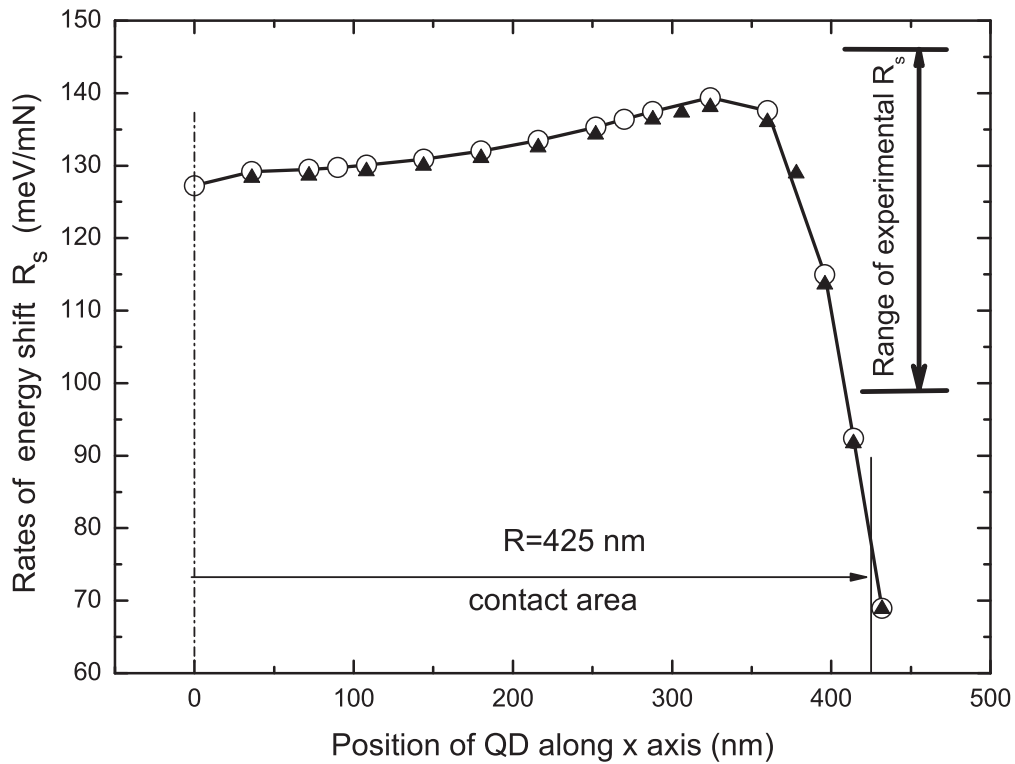


**Fig. 9** Dependence of the energy shift rates on the position of the QD along x direction. The line with open circles is the energy shift rates of QDs with uniform In-distribution. The solid triangles are the energy shift rates of QDs with the linear indium distribution of 74% at top and 44% at the base.



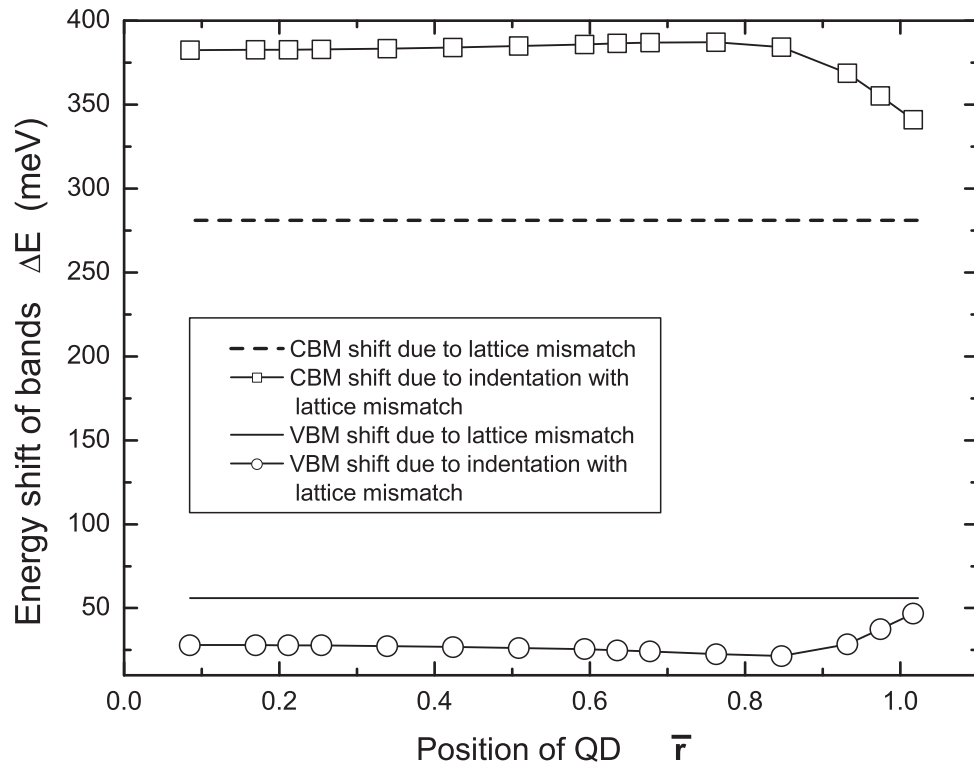


**Fig. 10** Dependence of energy shift of conduction band minimum (CBM) and valence band maximum (VBM) on the position of the QD along x axis.

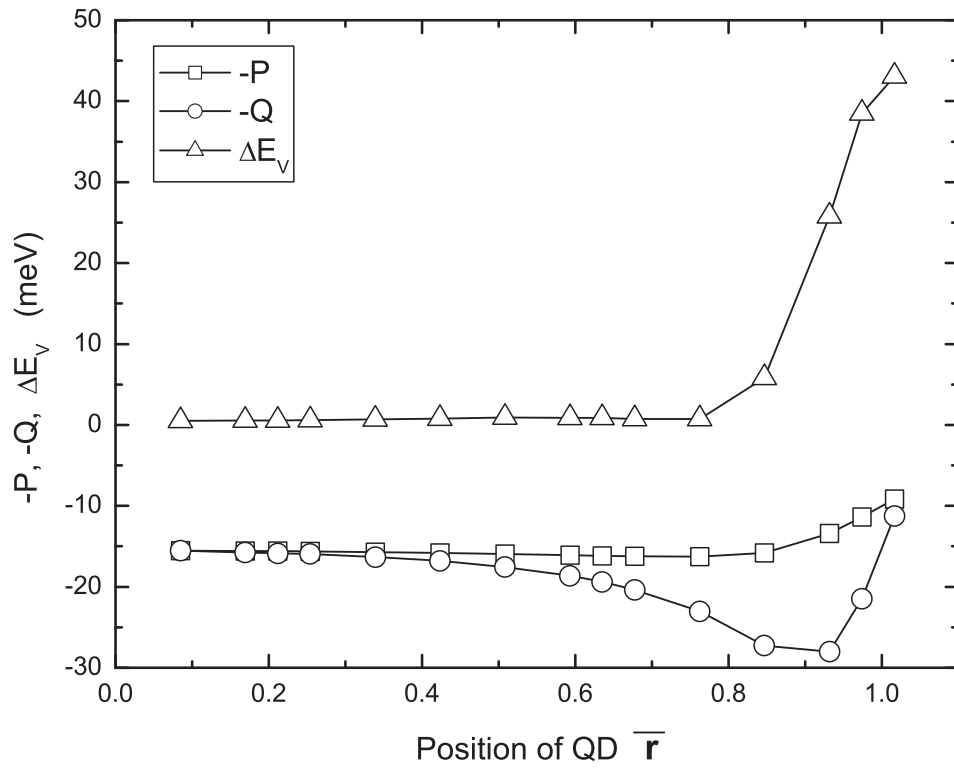


**Fig. 11 Dependence of  $-P$ ,  $-Q$  and  $\Delta E_V$  on the position of the QD due to 1.0 mN indentation force.**

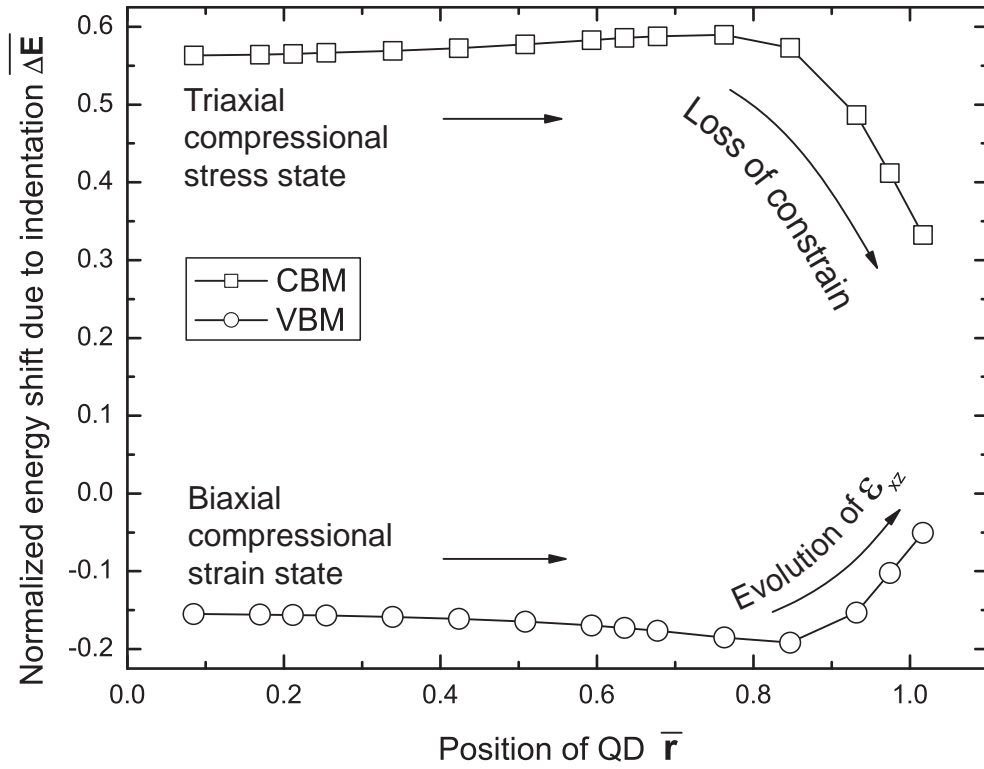


**Fig. 12** Dependence of shifts of the CBM and the VBM on the position of the QD, the shifts are the difference of lattice mismatch case and superposition of indentation force with lattice mismatch case.

Table1. Material parameters used in the calculation of strain and energy band shift.

	GaAs	In <sub>0.5</sub> Ga <sub>0.5</sub> As	Quartz
$a(\text{\AA})$	5.6533	5.8558	-
$c_{11}(\text{GPa})$	118.8	101.05	-
$c_{12}(\text{GPa})$	53.8	49.53	-
$c_{44}(\text{GPa})$	59.4	49.49	-
$a_c(\text{eV})$	-7.63	-6.06	-
$a_v(\text{eV})$	-1.00	-0.93	-
$b(\text{eV})$	-1.77	-1.81	-
$d(\text{eV})$	-3.10	-3.21	-
$\Delta_0(\text{eV})$	0.33	0.35	-
E (Young's modulus , GPa)	-	-	73.1
$\nu$ (Poisson's ratio)	-	-	0.17